Spatial resolution assessment in confocal Raman microscopy using two-dimensional materials and the underlying Si substrate

Zhong-Jie Wang(王钟杰), Tao Liu(刘涛), Xue-Lu Liu(刘雪璐), Miao-Ling Lin(林妙玲), Ping-Heng Tan(谭平恒)

Citation: Chin. Phys. B. 35, 107802 (2026). DOI: 10.1088/1674-1056/ae881b | CSTR: 32038.14.CPB.ae881b
http://cpb.iphy.ac.cn; http://iopscience.iop.org/cpb

What follows is a list of articles you may be interested in

Unveiling localized electronic properties of ReS_2 thin layers at nanoscale using Kelvin force probe microscopy combined with tip-enhanced Raman spectroscopy

Yu Luo(罗宇), Weitao Su(苏伟涛), Juanjuan Zhang(张娟娟), Fei Chen(陈飞), Ke Wu(武可), Yijie Zeng(曾宜杰), Hongwei Lu(卢红伟)

Chin. Phys. B. 32, 117801 (2023). DOI: 10.1088/1674-1056/ace425

Influence of fluorescence time characteristics on the spatial resolution of CW-stimulated emission depletion microscopy

Haiyun Qin(秦海芸), Wei Zhao(赵伟), Chen Zhang(张琛), Yong Liu(刘勇), Guiren Wang(王归仁), Kaige Wang(王凯歌)

Chin. Phys. B. 27, 037803 (2018). DOI: 10.1088/1674-1056/27/3/037803

Josephson diode effect in altermagnet-based s-wave superconductor junction

Yi Jiang(蒋易), Han-Lin Liu(刘翰林), Jun Wang(汪军)

Chin. Phys. B. 34, 107803 (2025). DOI: 10.1088/1674-1056/add7aa | CSTR: 32038.14.CPB.add7aa

Effects of helium ion irradiation and thermal annealing on the optical and structural properties of hexagonal boron nitride

Guan-Lin Liu(刘冠麟), Ji-Lian Xu(徐辑廉), Peng-Tao Jing(景鹏涛), Jing-Jing Shao(邵京京), Xu Guo(郭旭), Yun-Tao Wu(吴韵涛), Feng Qin(覃凤), Zhen Cheng(程祯), Deming Liu(刘德明), Yang Bao(鲍洋), Hai Xu(徐海), Li-Gong Zhang(张立功), Da Zhan(詹达), Jia-Xu Yan(闫家旭), Lei Liu(刘雷), De-Zhen Shen(申德振)

Chin. Phys. B. 34, 057801 (2025). DOI: 10.1088/1674-1056/adbee7 | CSTR: 32038.14.CPB.adbee7

INSTRUMENTATION AND MEASUREMENT

Spatial resolution assessment in confocal Raman microscopy using two-dimensional materials and the underlying Si substrate

Zhong-Jie Wang(王钟杰)[1,2], Tao Liu(刘涛)[1,2], Xue-Lu Liu(刘雪璐)[1,2], Miao-Ling Lin(林妙玲)[1,2], and Ping-Heng Tan(谭平恒)[1,2,†]

[1] *State Key Laboratory of Semiconductor Physics and Chip Technologies, Institute of Semiconductors, Chinese Academy of Sciences, Beijing* 100083, *China*

[2] *Center of Materials Science and Optoelectronics Engineering, University of Chinese Academy of Sciences, Beijing* 100049, *China*

(Received 19 April 2026; revised manuscript received 7 July 2026; accepted manuscript online 9 July 2026)

Confocal Raman microscopy is a powerful tool for micro/nano-scale characterization, yet a systematic and quantitative method to assess its spatial resolution — encompassing both lateral (LSR) and axial (ASR) dimensions — remains a critical challenge, particularly in understanding how atomically thin materials compare to bulk substrates as reference standards. Here we present a comprehensive methodology integrating Gaussian beam modeling with experimental cross-edge and z-axial Raman scans on graphene and MoS_2 flakes deposited on SiO_2/Si substrates. By quantitatively analyzing the Raman intensity profiles of the two-dimensional materials and the underlying Si substrate, we elucidate the distinct influences of the substrate's optical penetration depth and the two-dimensional nature of the flakes on LSR and ASR measurements. Our findings reveal a critical distinction between the two materials: graphene flakes (monolayer and multilayer) serve as a universal LSR calibration standard, whereas MoS_2's suitability is confined to monolayer and bilayer forms, as thicker flakes are compromised by edge-induced Raman enhancement. The Si substrate yields larger LSR values but ASR values comparable to those from two-dimensional flakes. This work establishes a robust framework for spatial resolution assessment, clarifies the role of pinhole size, and provides critical insights for optimizing the performance of confocal Raman microscopy.

Keywords: confocal Raman microscopy, spatial resolution, two-dimensional materials, Gaussian beam model

PACS: 78.30.–j, 78.67.–n, 87.57.cf, 81.05.ue

DOI: 10.1088/1674-1056/ae881b **CSTR:** 32038.14.CPB.ae881b

1. Introduction

Confocal Raman spectroscopy, as a powerful and efficient characterization technique, is widely employed in materials studies.[1–4] The conjugate pinhole, invented by Marvin Minsky,[5] enables confocal Raman microscopy to achieve spatial filtering and provide three-dimensional spatial resolution. The spatial resolution of a confocal Raman microscope serves as a key performance metric, directly determining its capability for precise analysis of materials at the micro/nano scales.[6–11] This metric comprises two interrelated dimensions: lateral spatial resolution (LSR) and axial spatial resolution (ASR). The LSR defines the system's ability to distinguish between two adjacent points in the X–Y plane and governs its accuracy in resolving fine surface morphology[12,13] and chemical composition distribution,[14,15] while the ASR characterizes the instrument's discrimination capability along the Z axis. High spatial resolution makes confocal Raman technology indispensable in cutting-edge fields,[13,16–19] providing critical technical support for understanding structure–property relationships at micro/nano scales. Consequently, developing quantitative methods for spatial resolution measurement is essential not only for evaluating system performance and optimizing experimental design, but also for supporting theoretical models and advancing next-generation devices.[17]

In optical systems, diffraction effects limit the imaging of a point source to a blurred spot, whose intensity distribution is described by the point spread function (PSF).[20] For a non-confocal Raman microscopy system—where the pinhole is sufficiently large, the LSR is quantitatively described by the Rayleigh criterion

$$\mathrm{LSR}_{\text{non-cf}} = \frac{0.61\lambda_{\mathrm{ex}}}{\mathrm{NA}}, \tag{1}$$

where λ_{ex} is the excitation wavelength, and NA is the numerical aperture of the objective. In a confocal Raman microscope equipped with a point detector, the effective PSF is given by the convolution of the excitation PSF and the detection PSF. As the pinhole size approaches zero, approximating an ideal point detector, the effective PSF can be approximated as the product of the excitation and detection PSFs. Under this condition, the diffraction-limited LSR becomes[20]

$$\mathrm{LSR}_{\mathrm{cf}} = \frac{1}{\sqrt{1+(\lambda_{\mathrm{ex}}/\lambda_{\mathrm{det}})^2}} \cdot \frac{0.61\lambda_{\mathrm{ex}}}{\mathrm{NA}}, \tag{2}$$

†Corresponding author. E-mail: phtan@semi.ac.cn

© 2026 Chinese Physical Society and IOP Publishing Ltd. All rights, including for text and data mining, AI training, and similar technologies, are reserved.

where λ_{det} is the detection wavelength. The Rayleigh criterion can also be extended to describe the ASR of a Raman microscope. For a non-confocal Raman microscopy system, the axial resolution is determined by the axial extent of the PSF along the optical axis. The corresponding ASR is given by[20]

$$\mathrm{ASR}_{\mathrm{non-cf}} = \frac{2n\lambda_{\mathrm{ex}}}{\mathrm{NA}^2}, \tag{3}$$

where n is the medium refractive index, e.g., air. For a confocal Raman microscope, the axial resolution is improved due to the convolution of the excitation and detection PSFs. Under the confocal condition, the diffraction-limited ASR becomes[20]

$$\mathrm{ASR}_{\mathrm{cf}} = \frac{1}{\sqrt{1+(\lambda_{\mathrm{ex}}/\lambda_{\mathrm{det}})^2}} \cdot \frac{2n\lambda_{\mathrm{ex}}}{\mathrm{NA}^2}. \tag{4}$$

Equation (2) differs from the wrong formulas in previous work[21] because the numerical aperture ($\mathrm{NA} = n\sin\theta$) inherently accounts for the medium refractive index n. In practical Raman microscopy, however, effects such as the scattering of laser and Raman photons, along with interactions with sample interfaces, can reduce the effective spatial resolution. Moreover, under realistic experimental conditions, the choice of confocal aperture size may influence the effective LSR and ASR.

Several approaches have been proposed to evaluate the spatial resolution of confocal Raman microscopy. For LSR assessment, one common approach employs reference samples with sub-diffraction-limited features, such as nanoparticles,[22] carbon nanotubes,[21] and gold nanowires,[23] where the spatial spread of their Raman signals serves as an LSR benchmark. This method requires reference materials with strong Raman contrast and precisely defined dimensions, posing significant challenges in sample preparation and relocation under an optical microscope. An alternative method is the knife-edge technique,[24,25] which involves scanning the laser across a sharp material edge and analyzing the resulting Raman intensity profile to estimate the spot size. While this method avoids the need for specialized calibration samples, it is susceptible to edge-related artifacts[26–29] that may compromise both modeling and measurement accuracy. Two-dimensional materials (2DMs), owing to their atomic-scale thickness, atomically sharp edges, and strong Raman signals, have emerged as ideal platforms for LSR measurement. Recently, a study[30] used graphene edges to probe the focal volume of Raman microscopes. In addition, a work using cross-edge scanning of the graphene D mode has demonstrated lateral resolution values approaching the theoretical diffraction limit.[31] Given the weak Raman intensity of the graphene D mode, it is desirable to develop a more general method for probing LSR using other atomically thin 2DMs and the underlying Si substrate.

For ASR assessment, measurements typically rely on fluorescence from small beads,[32,33] which may not directly correspond to that in Raman imaging. Stringent requirements regarding sample size and distribution further complicate sample preparation. Moreover, this method often yields a smaller measured axial resolution for small particles compared to planar samples, as the signal from a point source lacks contributions from regions adjacent to the optical axis. de Grauw *et al.*[34] used a single-lens model and calculated the integral of the Gaussian beam at the pinhole to obtain the axial response of a confocal Raman microscope. Polystyrene films[34] and graphene[21,30,35] have been used for ASR measurements, but these methods impose specific requirements on sample preparation, and the measurement conditions do not approach the optimal confocal regime. Due to the large depth of focus of Gaussian beams, in principle, 2DMs and their underlying Si substrate could also be employed for ASR determination. However, the corresponding theoretical models require further development. Therefore, establishing a model for the spatial distribution of Raman signal intensity and developing simple yet reliable methods using reference samples with strong Raman signals are essential for accurate spatial resolution assessment.

In this study, we systematically investigated the lateral and axial spatial resolutions of confocal Raman microscopy by analyzing Raman intensity profiles acquired from cross-edge scans at the edges of MoS_2 and graphene flakes deposited on SiO_2/Si substrates, as well as from z-axial Raman scans. By employing a Gaussian beam model for quantitative analysis, we elucidated the dependence of LSR and ASR on pinhole size and established a direct comparison between atomically thin two-dimensional materials and the underlying Si substrate as reference samples for spatial resolution assessment. Our results demonstrate that mono- and multi-layer graphene flakes are universally suitable for LSR calibration, whereas only monolayer and bilayer MoS_2 are appropriate due to the edge-related hot-spot effects in thicker flakes. The LSR values deduced from the Si substrate were considerably larger than those obtained from 2DM flakes, attributable to the combined effects of the SiO_2 spacer layer and the finite optical penetration depth in the Si substrate. In contrast, the ASR values derived from the Si substrate showed good agreement with those from 2DM flakes for larger (> 80) pinhole sizes. This work not only reveals how pinhole size governs both LSR and ASR but also offers a more accurate, practical, and well-justified framework for predicting and measuring axial resolution in confocal Raman microscopy.

2. Experimental methods

Graphene flakes were mechanically exfoliated from bulk crystals and directly deposited onto 90 nm SiO_2/Si substrates. MoS_2 flakes were first exfoliated onto a polydimethylsiloxane (PDMS) sheet and then transferred onto the 90 nm SiO_2/Si substrate using an all-dry viscoelastic stamping technique.[36] The numbers of layers in graphene and MoS_2 flakes were determined from the intensity of the Si Raman signal.[37,38] Raman spectroscopy was performed in a backscattering configuration using a Horiba HR800 confocal Raman microscope equipped with an edge filter and a charge-coupled device (CCD) detector. The confocal pinhole size of this system can be automatically adjusted within a range of 10–250 μm. Room-temperature spectra were acquired using a 100× objective (NA = 0.90). Excitation was provided by a 532 nm diode-pumped solid-state laser (output power: 40 mW). The power delivered to the sample was reduced below 0.5 mW for graphene[39] and 0.2 mW for MoS_2,[40] measured below the objective, to minimize laser-induced heating. Proper focusing on the sample plane was achieved by performing a z-axis scan to maximize the intensity of the respective Raman mode, specifically the A_1' mode for MoS_2 and the G mode for graphene, which is a sensitive and reliable indicator of optimal focal position for 2DM. For LSR measurements, a step size of 0.05 μm was employed using the P-733.2CD stage (Physik Instrumente SE & Co. KG), while for ASR measurements, a step size of 0.2 μm was used with the SCANplus 75×50 stage (Märzhäuser Wetzlar GmbH & Co. KG). These step sizes were verified using a stage micrometer. The peak area was used to model the intensity profile.

3. Theoretical model

In microscopy and optical systems, the laser beam is predominantly modeled as a Gaussian beam, as it accurately represents the fundamental transverse mode (TEM_{00}) emitted by most lasers. This mode exhibits a smooth, radially symmetric intensity profile that minimizes diffraction effects and enables the tightest possible focusing, which is a critical requirement for achieving high spatial resolution in applications such as confocal Raman microscopy. Moreover, the well-defined mathematical framework describing Gaussian beam propagation allows for precise control and prediction of beam parameters throughout the optical path. In our setup, the beam is expanded to overfill the objective entrance pupil to achieve the nominal numerical aperture. However, truncation at the objective entrance pupil can induce diffraction effects, causing the actual beam intensity distribution to approach an Airy pattern.[41] Nevertheless, in our experimental configuration, the truncation is not severe, and it is widely recognized in optics that the Gaussian function serves as a good approximation of the Airy pattern.[30] Therefore, using a Gaussian beam model is scientifically justified. In the following analysis, we employ a Gaussian beam model to quantitatively characterize the lateral and axial Raman intensity distributions for both multilayer flakes and the underlying Si substrate.

3.1. Lateral spatial resolution

To analyze the spatial resolution of a Raman spectrometer, it is essential to determine the intensity distribution of the excitation laser. The laser beam is modeled as having a Gaussian intensity profile. In the focal plane (defined as $z = 0$), the intensity is maximum at the beam center and decreases gradually with radial distance, as described by the equation[42]

$$I(x,y) = I_0 \exp\left(-\frac{2\left((x-x_c)^2+(y-y_c)^2\right)}{r_0^2}\right), \tag{5}$$

where I_0 is the peak intensity at the beam center, (x,y) are the coordinates of a point in the focal plane, and (x_c,y_c) are the coordinates of the beam center. The beam waist radius (r_0) of the Gaussian beam is defined as the distance from the beam center to the point at which the intensity I drops to $1/e^2$ of I_0, which corresponds to the spot size of the Gaussian laser beam at the sample plane.

For 2DMs, due to their atomic-scale thickness, the intensity of most Raman modes is sensitive to the laser-illuminated area. Therefore, the corresponding Raman intensity can be obtained by integrating the laser intensity distribution over the illuminated region on the 2DM:[31]

$$I_{2DM}(x) \propto \frac{2}{\sqrt{2\pi}r_0}\int_0^{\infty} \exp\left(-\frac{2(x'-x)^2}{r_0^2}\right) dx', \tag{6}$$

where x is the distance from the beam center to the edge of the 2DM.

The Raman signal from the Si substrate originates from both the exposed substrate region and the area covered by the 2DM, as illustrated in Fig. 1(a). To account for this, a spatial masking function $M(x')$ is introduced to describe the transmittance distribution:

$$M(x') = \begin{cases} 1, & x' < 0, \\ T, & x' > 0, \end{cases} \tag{7}$$

where $0 < T < 1$ is the transmission coefficient through the 2DM flake. Accordingly, the intensity of the Si substrate during cross-edge Raman scan at the edge of the 2DM flake, I_{Si-2DM}, can be expressed as

$$\begin{aligned} I_{Si-2DM}(x) &\propto \int_{-\infty}^{+\infty} M(x') \cdot \exp\left(-\frac{2(x'-x)^2}{r_0^2}\right) dx' \\ &\propto 1 - \frac{2(1-T)}{\sqrt{2\pi}r_0}\int_0^{+\infty} \exp\left(-\frac{2(x'-x)^2}{r_0^2}\right) dx', \end{aligned} \tag{8}$$

where x is again the distance from the beam center to the edge of the 2DM flake.

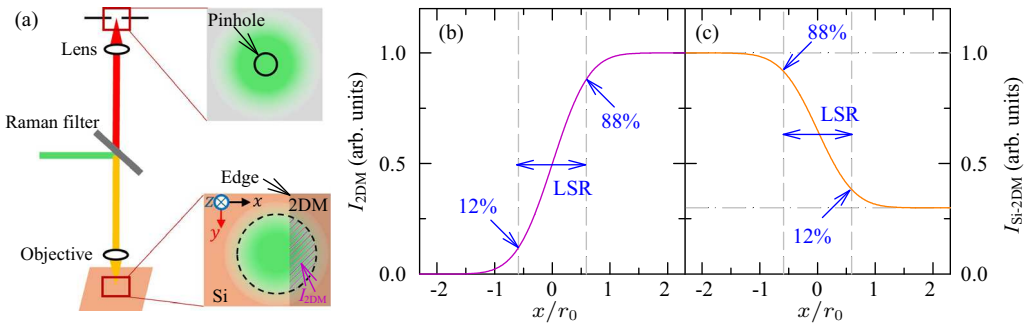

Fig. 1. (a) Schematic of the simplified optical path illustrating the projection of the Gaussian beam at the pinhole and 2DM planes. (b) Normalized I_{2DM} and (c) normalized I_{Si-2DM} as functions of the normalized laser beam position x/r_0 relative to the sample edge.

Figures 1(b) and 1(c) show the calculated normalized intensity profiles I_{2DM} and I_{Si-2DM} as functions of the normalized beam position x/r_0 when the laser beam scans across the 2DM edge. The profiles are obtained from Eqs. (6) and (8), respectively, with a transmission coefficient of $T = 0.3$ used in Eq. (8). The experimental LSR (LSR_{exp}) is determined as the lateral distance between the 12% and 88% relative intensity points in the respective Raman intensity profiles across the edge, following the convention of the knife-edge method.[43] Alternatively, LSR (LSR_{exp}) can be obtained by fitting the experimental cross-edge Raman intensity profiles to the model described in Eq. (6) or Eq. (8) to extract the beam waist radius r_0, and then calculating $LSR_{exp} = \sqrt{2\ln 2}r_0$.

3.2. Axial spatial resolution

The axial resolution requires consideration of a more complex optical model. As mentioned previously, the intensity of the Raman signal is determined by the integrated laser intensity within the sample plane. While the total power of a Gaussian beam is conserved across transverse planes, the signal intensity actually collected in a confocal system is limited by the size of the pinhole. Although de Grauw *et al.*[34] derived the variation of collected signal intensity with defocus using a single-lens model and Gaussian beam theory, the single-lens model is far from sufficient for practical confocal Raman microscopes due to their complexity. Therefore, we establish a double-lens model. We model the optical path of a confocal Raman microscope using a lens assembly comprising an objective and a focusing lens, which better represents the actual optical path in a commercial confocal Raman microscope, as illustrated in Fig. 2(a). In this configuration, the objective and focusing lenses are arranged confocally, with the distance between the focusing lens and the pinhole equal to the focal length (f) of the focusing lens. Although a real objective consists of multiple lens elements to correct chromatic and spherical aberrations, since both the laser and Raman signals are monochromatic, it is reasonable to approximate the objective as a single lens with the same NA and focal length (f). It should be noted that in non-air media (e.g., oil), the effective focal length of the objective would change and spherical aberrations would become significant, which complicates the optical propagation. Therefore, our model is specifically established for air media, which covers the vast majority of practical applications of confocal Raman microscopy. When the laser focuses on the sample, the beam waist of the excitation light lies at the sample plane, while that of the Raman signal from the sample is located at the pinhole plane. The excitation beam waist radius r_0 and the Raman signal beam waist radius r_0' are related by the optical system magnification as follows:

$$r_0' = \frac{M_0 L_2}{L_1} r_0, \tag{9}$$

where M_0 is the nominal magnification of the objective lens, and L_1 and L_2 are the tube lengths of the objective and focusing lenses, respectively.

When the laser focal plane is misaligned with the sample plane by a distance z (where z is negative when the distance between the objective and the sample plane exceeds the focal length of the objective), the corresponding Gaussian beam radius $r(z)$ can be expressed as[42]

$$r(z) = r_0 \sqrt{1 + \left(\frac{z\lambda_{ex}}{\pi r_0^2}\right)^2}. \tag{10}$$

For an object distance of $s_1(z) = f - z$, the thin lens formula gives the image distance $i_1(z)$ as

$$i_1(z) = \frac{f(f-z)}{z}, \tag{11}$$

where f is the focal length of the objective lens. With $s_2(z) = L_1 + L_2 - i_1(z)$ as the object distance for the focusing lens, the corresponding image distance $i_2(z)$ follows

$$i_2(z) = \frac{(L_1+L_2)f'z + (f-z)f}{(L_1+L_2-f')z + (f-z)f'}, \tag{12}$$

where f' is the focal length of the focusing lens. The actual magnification $M(z)$ of the system is

$$M(z) = -\frac{ff'}{z^2(L_1+L_2+f-f') + zf^2}. \tag{13}$$

The beam waist radius after the focusing lens is given by $r'(z) = M(z) \cdot r(z)$. Since the beam maintains its Gaussian

characteristics upon transmission through the focusing lens, the distance $z'(z)$ from the beam waist plane to the pinhole location is

$$z'(z) = i_2(z) - f'. \tag{14}$$

Therefore, the corresponding Gaussian beam radius at the pinhole plane $r'_{\mathrm{at-ph}}(z)$ can be expressed as

$$r'_{\mathrm{at-ph}}(z) = r'(z)\sqrt{1+\left(\frac{z'(z)\lambda_{\mathrm{det}}}{\pi[r'(z)]^2}\right)^2}. \tag{15}$$

The Raman signal intensity distribution at the pinhole plane is

$$I'(z) = I'_0(z)\exp\left[-\frac{2R^2}{[r'_{\mathrm{at_ph}}(z)]^2}\right], \tag{16}$$

where $I'_0(z) = I_0 \cdot r_0^2/[r'_{\mathrm{at_ph}}(z)]^2$ is the intensity at the center of the pinhole plane, and R is the radial distance from the pinhole center. The detected Raman signal intensity is determined by integrating the intensity distribution of the incident beam over the pinhole area. We obtain for the intensity throughput through the pinhole:

$$\begin{aligned} I(z) &= \int_0^{2\pi}\int_0^{r_{\mathrm{ph}}} I'(z)\,\mathrm{d}R\,\mathrm{d}\theta \\ &\propto 1-\exp\left(-\frac{2r_{\mathrm{ph}}^2}{[r'_{\mathrm{at_ph}}(z)]^2}\right), \end{aligned} \tag{17}$$

where r_{ph} is the pinhole radius and C is a constant.

By systematically varying the defocus distance z and the pinhole size, the axial intensity distribution of the Raman signal is obtained, as shown in Figs. 2(b1) and 2(b2). When the projected beam radius at the pinhole plane satisfies $r_{\mathrm{ph}} < r'_0$, even at optimal focus, a portion of the signal is blocked by the pinhole. As z increases, the beam radius at the pinhole expands further, leading to increased signal rejection and a corresponding decrease in detected intensity. In contrast, when $r_{\mathrm{ph}} > r'_0$, nearly the entire signal is collected within a small axial displacement, resulting in a plateau at the peak of the axial intensity profile. The full width at half maximum (FWHM) of the axial intensity profile is conventionally defined as the calculated ASR ($\mathrm{ASR_{cal}}$).[34] As the pinhole size increases, $\mathrm{ASR_{cal}}$ progressively degrades. The axial intensity profile exhibits a noticeable asymmetry in its lineshape, which arises from the inherent asymmetry of the object-image conjugation in lens-based imaging systems. Figure 2(c) shows the dependence of $\mathrm{ASR_{cal}}$ on pinhole size. Initially, $\mathrm{ASR_{cal}}$ increases slowly with pinhole size and then rises in an approximately linear manner. As the pinhole size approaches infinity, $\mathrm{ASR_{cal}}$ also tends to infinity, indicating a loss of axial sectioning capability and an inability to resolve different layers along the optical axis. In this regime, the axial intensity profile flattens into a horizontal line, consistent with the model assumptions.

For experimental measurements, the on-axis intensity of an ideal Gaussian beam follows a Lorentzian axial distribution.[44] However, due to beam truncation at the objective entrance pupil, the axial distribution of the diffracted Gaussian beam approaches an Airy pattern.[41] Therefore, using a purely Lorentzian function to fit the experimental data would be inappropriate. Considering that the truncation is not severe and a Lorentzian component remains in the axial distribution, together with the approximately Gaussian profile in the lateral plane, a Voigt function is employed to fit the experimental data[21] to extract the FWHM as the experimentally measured ASR ($\mathrm{ASR_{exp}}$).

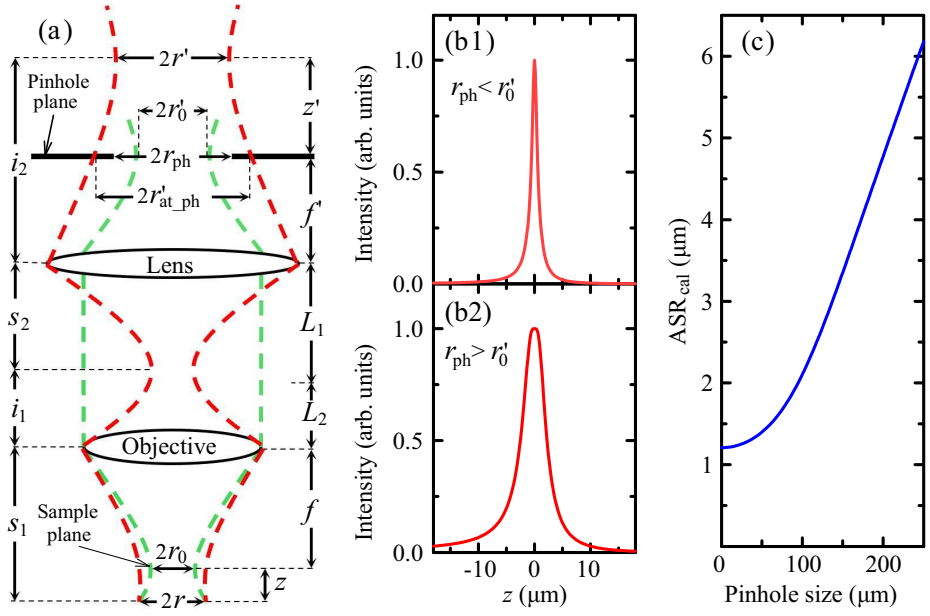

Fig. 2. (a) Schematic illustration of the optical collection path in a confocal Raman microscope under focused (green) and defocused (red) conditions. (b1), (b2) Schematic plots of the normalized axial Raman intensity distribution as a function of the defocus distance z for (b1) $r_{\mathrm{ph}} < r'_0$ and (b2) $r_{\mathrm{ph}} > r'_0$. (c) Example of the calculated axial spatial resolution ($\mathrm{ASR_{cal}}$) as a function of pinhole size.

It is worth noting that Eq. (17) in our double-lens model shares a similar mathematical structure with the corresponding equation in the single-lens model,[34] our double-lens model offers the following improvements: 1) It derives explicit expressions for the beam waist at the pinhole plane as a function of defocus z, incorporating the effect of image distance variation via the thin-lens equation and the change of magnification with z. 2) It provides a clear formula linking r_0 (excitation waist) and r_0' (signal waist at the pinhole) using the objective magnification M_0 and tube lengths L_1 and L_2. 3) It derives $M(z)$ explicitly as a function of z, including the combined effect of the objective and the focusing lens. 4) It introduces λ_{det} explicitly in the propagation after the focusing lens as shown in Eq. (15), thereby separating excitation and detection wavelengths, a refinement not present in earlier models. 5) It clearly states that when $r_{\mathrm{ph}} > r_0'$, a plateau appears in the axial response because the entire in-focus signal passes through the pinhole. In short, the double-lens model lies in the more realistic optical modeling, better fitting functions, and systematic experimental validation using modern two-dimensional material standards, which together provide a more accurate and practical framework for predicting and measuring ASR in confocal Raman microscopy.

4. Results and discussion

In bulk crystals, the Raman signal originates from a finite volume comparable to the optical penetration depth, which complicates the treatment of the sample as an ideal two-dimensional object in the focal plane for spatial resolution analysis in confocal Raman microscopy. In contrast, 2DMs possess atomic-scale thickness, making them well-suited as model systems for spatial resolution studies. In the following analysis, we examine Raman intensity profiles acquired from cross-edge Raman scans at the edges of 2DM flakes deposited on SiO_2/Si substrates, as well as from z-axial Raman scans. The goal is to elucidate the differences between 2DMs and the underlying Si substrate as reference samples for spatial resolution measurements based on a Gaussian beam model.

4.1. Lateral spatial resolution

To validate the aforementioned model, we performed cross-edge Raman scan measurements at the edges of n-layer graphene (nLG, $n = 1, 6, 10$) and m-layer MoS_2 (mLM, $m = 1, 2, 5$) flakes deposited on SiO_2/Si substrates under a pinhole size of 20 μm. The corresponding Raman spectra at the basal plane of nLG and mLM are shown in Figs. 3(a) and 3(b), respectively. The G mode of nLG and the A_1' of mLM are labeled, with their Raman intensities denoted as $I_{\mathrm{G-nLG}}$ and $I_{\mathrm{A-mLM}}$, respectively.

For cross-edge Raman scan measurements, only flakes with optically straight and clean edges were selected under the optical microscope (100× objective) to minimize the influence of edge roughness on the measured LSR. To further verify the edge quality, we performed AFM measurements on the 10LG flake. The AFM image (inset in Fig. 3(c3)) confirms that the flake exhibits a smooth surface and a sharp edge, with edge roughness within 20 nm, far smaller than the diffraction-limited laser spot size, and thus does not affect our LSR measurements. No micron-scale undulations or wrinkles were observed in the scanned region. In addition, no strain-induced Raman peak shifts or splitting were observed in any of our samples, which further confirms the flatness and uniformity of the flakes. Figures 3(c1), 3(c2), and 3(c3) show the $I_{\mathrm{G-nLG}}$ profiles measured across the edges of 1LG, 6LG, and 10LG, respectively. Each $I_{\mathrm{G-nLG}}$ profile exhibits a characteristic sigmoidal shape. Fitting these profiles with Eq. (6) yields $\mathrm{LSR_{exp}}$ values of 0.27 μm, which are in good agreement with previously reported results[31] and with the diffraction-limited lateral spatial resolution for a confocal Raman microscope, $\mathrm{LSR_{cf}}$, calculated using Eq. (2). This result is quite natural because even for 10LG, the thickness is only about 3.4 nm, which is far smaller than the micron-scale Rayleigh length. Therefore, the Raman intensity can still be considered as proportional to the illuminated area.

Figures 3(d1), 3(d2), and 3(d3) depict the $I_{\mathrm{A-mLM}}$ profiles measured across the edges of 1LM, 2LM, and 5LM, respectively. The $I_{\mathrm{A-mLM}}$ profiles of 1LM and 2LM exhibit similar sigmoidal behavior to those observed for nLG. Fitting these profiles using Eq. (6) yields the same $\mathrm{LSR_{exp}}$ value of 0.27 μm. However, the A_1' mode of 5LM shows a noticeable intensity enhancement at the sample edge, as shown in Fig. 3(d3), which leads to a distorted $\mathrm{LSR_{exp}}$ result. It should be emphasized that such edge-related enhancement is not observed for 1LM, 2LM, or nLG ($n \leq 10$). Previous studies on bulk GaAs and black phosphorus flakes have reported similar intensity enhancements at sample edges, attributed to the formation of optical "hot spots" resulting from the redistribution of electromagnetic fields and the modification of wave propagation near the edge.[27] The physical mechanism underlying the absence of such hot spots at the edges of 1LM, 2LM, and nLG flakes warrants further investigation. This edge-induced enhancement directly interferes with accurate LSR determination, as the fitted intensity profile no longer reflects the true Gaussian beam profile. Therefore, when using MoS_2 flakes for LSR measurement, only monolayer and bilayer flakes are suitable. In contrast, graphene flakes with up to at least 10 layers do not exhibit such edge enhancement, which we attribute to their different dielectric response and weaker electromagnetic field confinement near the edge. This makes multilayer flake a more robust and practical choice for LSR measurements, especially considering its stronger Raman signal and ease of preparation compared to monolayers. When using the edges of 2DM flakes for LSR measurements, it is essential to verify whether edge-induced intensity enhancement of Raman modes occurs.

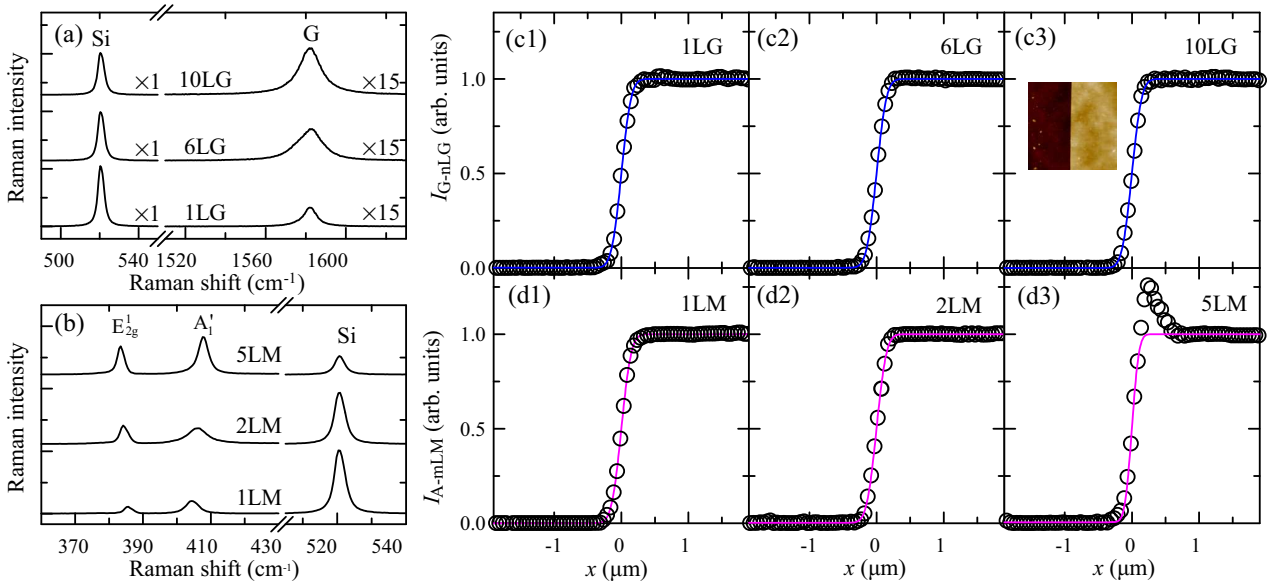

Fig. 3. (a) Raman spectra acquired from the basal plane of 1LG, 6LG, and 10LG flakes. (b) Raman spectra acquired from the basal plane of 1LM, 2LM, and 5LM flakes. (c) $I_{\mathrm{G-nLG}}$ as a function of the laser beam position x relative to the sample edge for 1LG, 6LG, and 10LG. (d) $I_{\mathrm{A-mLM}}$ as a function of the laser beam position x relative to the sample edge for 1LM, 2LM, and 5LM. All measurements were performed with a pinhole size of 20 μm. The circles represent the experimental data, and the solid lines are fits to Eq. (6).

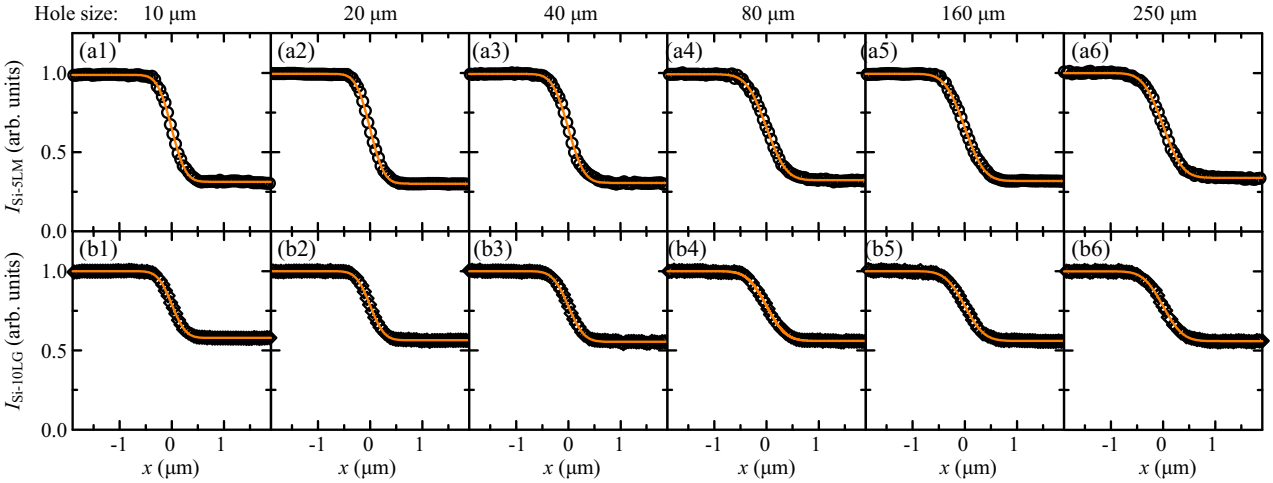

Fig. 4. (a) $I_{\mathrm{Si-5LM}}$ and (b) $I_{\mathrm{Si-10LG}}$ as functions of the lateral position x of the laser beam relative to the sample edge, measured with pinhole sizes of 10 μm, 20 μm, 40 μm, 80 μm, 160 μm, and 250 μm. The circles and diamonds represent the experimental data, and the solid lines are fits to Eq. (8).

To further investigate the influence of pinhole size on LSR, cross-edge Raman scan measurements of G mode were performed at the edge of a 10LG flake with pinhole sizes ranging from 10 μm to 250 μm. The fitted $\mathrm{LSR_{exp}}$ values gradually increase with pinhole size and tend to stabilize once the pinhole exceeds a certain diameter, as summarized in Table 1. This behavior is attributed to the broadening of the effective PSF with increasing pinhole size, causing the LSR to progressively approach that of non-confocal Raman microscopy.[45] At pinhole sizes of 10 μm and 20 μm, $\mathrm{LSR_{exp}}$ closely matches the diffraction-limited confocal value $\mathrm{LSR_{cf}}$, and is improved by a factor of approximately $\sqrt{2}$ compared to $\mathrm{LSR_{exp}}$ measured with larger pinholes (80 μm, 160 μm and 250 μm), which correspond to the non-confocal case $\mathrm{LSR_{non-cf}}$. Therefore, a pinhole size of 20 μm can be considered suitable for $\mathrm{LSR_{cf}}$ measurements under confocal conditions, since further reducing the pinhole size to 10 μm would significantly attenuate the Raman signal without improving the lateral resolution.

Cross-edge Raman scan measurements of the intensity of the Si substrate at the edge of both 5LM ($I_{\mathrm{Si-5LM}}$) and 10LG ($I_{\mathrm{Si-10LG}}$) flakes were also performed with pinhole sizes ranging from 10 μm to 250 μm, as depicted in Figs. 4(a) and 4(b). The $\mathrm{LSR_{exp}}$ values for each pinhole size, obtained by fitting the data of $I_{\mathrm{Si-5LM}}$ and $I_{\mathrm{Si-10LG}}$ with Eq. (8), are consistent with each other, as summarized in Table 1. Furthermore, the $\mathrm{LSR_{exp}}$ measured with a 10 μm pinhole is approximately a factor of $\sqrt{2}$ better than that obtained with a 250 μm pinhole, mirroring the theoretical improvement of $\mathrm{LSR_{cf}}$ over $\mathrm{LSR_{non-cf}}$.

It should be noted that for each pinhole size, the $\mathrm{LSR_{exp}}$ values extracted from the $I_{\mathrm{Si-5LM}}$ and $I_{\mathrm{Si-10LG}}$ profiles are significantly larger than those obtained from the I_{A} and I_{G} profiles. This discrepancy can be attributed to two main factors.

First, the presence of the SiO_2 spacer layer causes the lateral extent of the laser spot sampled during the line scan to differ from the true beam waist radius at the focal plane. Second, due to the finite optical penetration depth of Si under 532 nm excitation (approximately 800 nm), the Raman signal originates from a volume beneath the surface rather than from an ideal two-dimensional plane. This volumetric sensitivity leads to the collection of out-of-focus signal contributions, which broaden the measured intensity profile and degrade the accuracy of the resolution measurement. Consequently, the LSR values derived from Si substrates systematically overestimate the true lateral resolution of the confocal system. In contrast, these effects are absent in atomically thin 2DM flakes, as their Raman signals arise exclusively from the two-dimensional plane with negligible out-of-focus contributions. This makes atomically thin 2DM flakes an ideal platform for measuring the LSR of a confocal Raman microscope.

Table 1. LSR_{exp} values obtained from fitting the I_{G-10LG} profiles with Eq. (6) and the I_{Si-5LM} and $I_{Si-10LG}$ profiles with Eq. (8) for pinhole sizes ranging from 10 μm to 250 μm, together with the corresponding LSR_{non-cf} and LSR_{cf}.

Pinhole size (μm)		0	10	20	40	80	160	250
LSR_{exp} (μm)	I_{G-10LG}	–	0.27	0.27	0.32	0.35	0.37	0.36
	I_{Si-5LM}	–	0.50	0.50	0.57	0.70	0.70	0.70
	$I_{Si-10LG}$	–	0.50	0.50	0.56	0.69	0.70	0.70
LSR_{non-cf} (μm)		0.361	–	–	–	–	–	–
LSR_{cf} (μm)		0.265	–	–	–	–	–	–

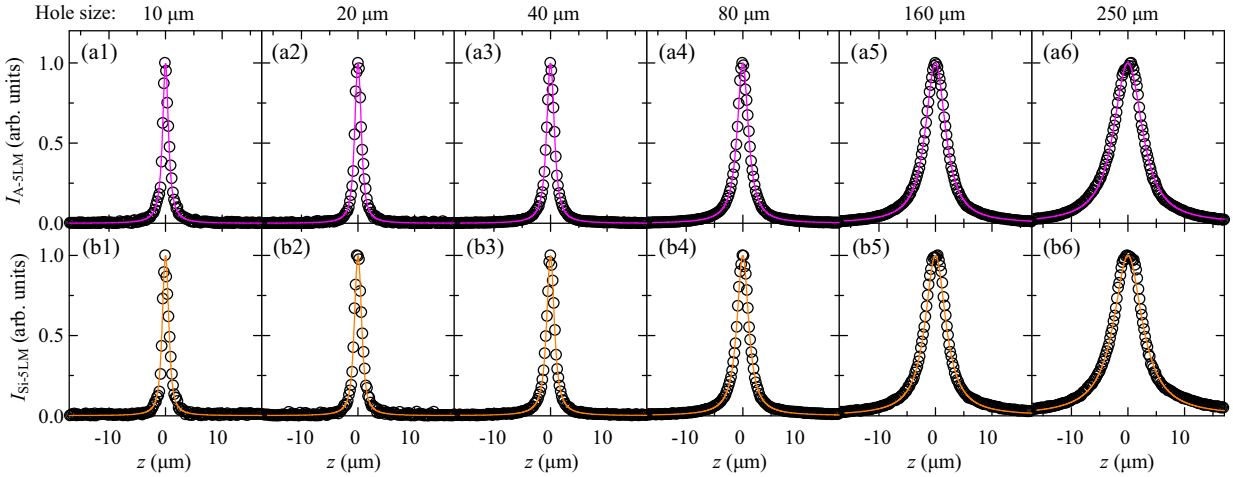

Fig. 5. (a) Axial profiles of I_{A-5LM} for 5LM, and (b) I_{Si-5LM} as functions of the defocus distance z, measured with pinhole sizes ranging from 10 μm to 250 μm. The circles represent the experimental data, and the solid lines are fits to the Voigt function.

4.2. Axial spatial resolution

For ASR measurement, we performed axial Raman scan measurements on 5LM and 10LG flakes deposited on a 90 nm SiO_2/Si substrate. The confocal Raman microscope consisted of an objective lens (NA = 0.9, 100×, 180 mm tube length) and a focusing lens (1.38×, 250 mm tube length). The axial intensity profiles of I_{A-5LM} and I_{Si-5LM} were measured as functions of the defocus distance z for pinhole sizes ranging from 10 μm to 250 μm, as shown by the scattered points in Fig. 5. These data were fitted using a Voigt function (solid lines in Fig. 5), and the resulting full widths at half maximum (FWHMs) were taken as the experimental axial spatial resolution (ASR_{exp}), summarized in Table 2. As the pinhole size increases, ASR_{exp} correspondingly increases. For pinhole sizes larger than 160 μm, the axial intensity profiles exhibit a nearly constant Raman signal near the focal plane ($z = 0$) and a slight asymmetry in lineshape. All the results are consistent with the theoretical analysis based on the Gaussian beam model.

Notably, the experimental ASR (ASR_{exp}) values obtained from the I_{A-5LM} and I_{G-10LG} profiles show good agreement across all pinhole sizes. For small pinhole sizes of 10 μm and 20 μm, the ASR_{exp} values extracted from the I_{Si-5LM} profile differ slightly from those determined from the I_{A-5LM} and I_{G-10LG} profiles. It is reasonable to attribute this discrepancy to the fact that pinhole sizes of 10 μm and 20 μm correspond to the true confocal regime, as also evidenced by the good agreement between LSR_{exp} and LSR_{cal} for these pinhole sizes. Although the penetration depth of the 532 nm laser in Si is approximately 0.8 μm, when the refractive index of Si is taken into account, an objective lens displacement of 0.1 μm corresponds to an optical path length inside the Si substrate comparable to this penetration depth.[46] For sufficiently large pinholes, the confocal z-sectioning effect is suppressed and the ASR becomes less sensitive to the sample-specific interface profiles. Thus, for pinhole sizes larger than 80 μm, it is expected that the ASR_{exp} values obtained from the I_{A-5LM}, I_{G-10LG} and I_{Si-5LM} profiles are in good agree-

ment with one another. It should also be noted that the calculated ASR (ASR_{cal}) is slightly smaller than the corresponding ASR_{exp}. This discrepancy can be attributed to the fact that the actual spot size in a confocal Raman system may deviate from the idealized calculation, as such systems are considerably more complex than a simple double-lens model.

To determine whether the substrate environment affects ASR measurements, we performed axial Raman scans on both the suspended 11LG ($11LG_{sus}$) and supported 11LG ($11LG_{sup}$) flakes mechanically exfoliated onto a SiO_2/Si substrate. The $11LG_{sus}$ flake was located over a circular aperture with a diameter of 6 μm and a depth of 1 μm. Figure 6(a) shows an optical image of the $11LG_{sus}$ and $11LG_{sup}$ flakes, and Fig. 6(b) compares the Raman spectra acquired from the $11LG_{sus}$ and $11LG_{sup}$ flakes. In both flakes, the G mode is located at approximately 1582 cm^{-1}, with no observable peak shift or linewidth broadening. These results indicate that both flakes have comparable sample quality, with no appreciable strain-induced spectral variation. Figures 6(c) and 6(d) show the axial G-mode intensity profiles of the $11LG_{sus}$ and $11LG_{sup}$ flakes, respectively, measured with a pinhole size of 20 μm. Voigt-function fits yield ASR_{exp} values of 1.39 μm for the $11LG_{sus}$ flake and 1.38 μm for the $11LG_{sup}$ flake, indicating close agreement between the two measurements. The measured ASR in our experiment is approximately 30% larger than the theoretical limit predicted by Eq. (4). It should be noted that a previous study has reported ASR values approaching the diffraction limit predicted by Eq. (4) using suspended monolayer graphene.[21] However, in their work, the value of the supported flake was not provided. Therefore, we cannot comment on the result. The close agreement between the $11LG_{sus}$ and $11LG_{sup}$ flakes in our work indicates that the substrate environment does not introduce a measurable change in the extracted ASR_{exp}. The corresponding results are summarized in Table 2 and are consistent with those obtained from 10LG and 5L MoS_2, further supporting the reproducibility of the ASR measurements across different two-dimensional reference samples.

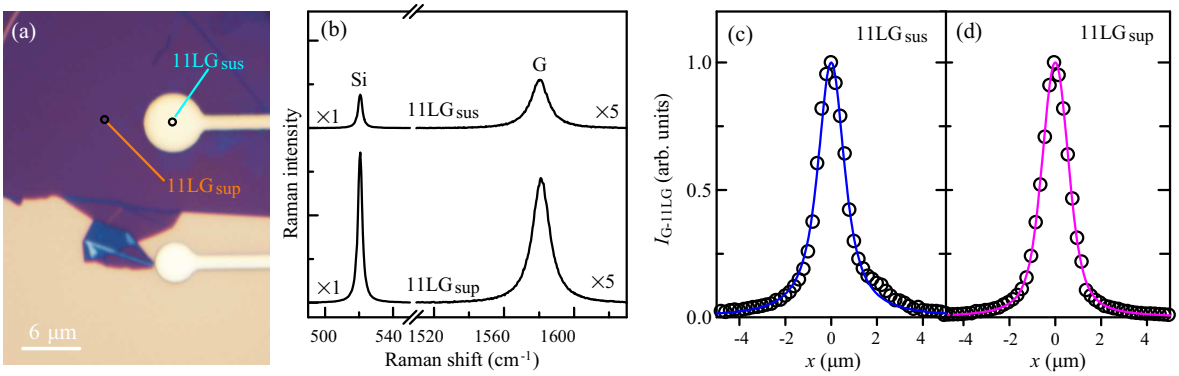

Fig. 6. (a) Optical image and (b) Raman spectra of the $11LG_{sus}$ and $11LG_{sup}$ flakes. (c), (d) Axial intensity profiles of I_{G-11LG} as a function of the defocus distance z, recorded with a pinhole size of 20 μm, for (c) the $11LG_{sus}$ flake and (d) the $11LG_{sup}$ flake. The circles denote the experimental data, and the solid curves represent Voigt-function fits to the measured profiles.

Table 2. ASR_{exp} values extracted from Voigt fits to the axial Raman intensity profiles of I_{A-5LM}, I_{G-10LG}, $I_{G-11LG-hole}$, $I_{G-11LG-sub}$, and I_{Si-5LM} measured with varying pinhole sizes, along with the corresponding ASR_{cal}, ASR_{non-cf} and ASR_{cf} values.

Pinhole size (μm)		0	10	20	40	80	160	250
ASR_{exp} (μm)	I_{A-5LM}	–	1.25	1.38	1.61	2.36	4.26	6.03
	I_{G-10LG}	–	1.24	1.37	1.65	2.44	4.31	6.06
	$I_{G-11LG_{sus}}$	–	–	1.39	–	–	–	–
	$I_{G-11LG_{sup}}$	–	–	1.38	–	–	–	–
	I_{Si-5LM}	–	1.37	1.49	1.62	2.47	4.37	6.10
ASR_{cal} (μm)		1.21	1.22	1.24	1.33	1.75	3.64	6.18
ASR_{non-cf} (μm)		1.33	–	–	–	–	–	–
ASR_{cf} (μm)		0.94	–	–	–	–	–	–

When the pinhole size is 10 μm, although the confocal condition is achieved, both ASR_{cal} and ASR_{exp} are larger than ASR_{cf}, which contrasts with the case of LSR. This behavior is physically expected. The lateral resolution has a sharp, physically defined cutoff (the first zero of the Airy disk), whereas the axial resolution lacks such a zero-crossing, as it is defined by a soft full-width-at-half-maximum value that depends on the signal-to-noise ratio rather than a hard physical boundary. Consequently, a microscope's LSR can reach the diffraction limit, but its ASR cannot. Although previous studies have noted that the entrance aperture of the objective lens can truncate the beam, causing the axial distribution of a Gaussian beam to become an Airy pattern after diffraction through the objective and thereby improving the ASR,[41] this truncation effect is very weak under our realistic experimental conditions, even after beam expansion. Consequently, the axial intensity

distribution does not follow an Airy pattern but instead resembles that of a realistic Gaussian beam, i.e., a Lorentzian function. This effect can therefore generally be neglected and has minimal impact on the experimental measurements. Notably, both our experimental and calculated ASR values at 10 μm remain smaller than ASR_{non-cf}, indicating that the confocal pinhole still provides a substantial improvement in axial sectioning capability even when the ideal diffraction limit is not fully attained.

Finally, the influence of flake thickness on ASR measurements should be considered. The Raman intensity I_{G-nLG} increases with the number of graphene layers up to approximately $n = 20$ for nLG flakes deposited on 90 nm SiO_2/Si substrates.[37] Therefore, multilayer graphene flakes can provide stronger Raman signals and reduce the acquisition time required for axial Raman scan measurements. Notably, even a 20LG flake, which yields the strongest Raman signal within this thickness range, is only approximately 7 nm thick and thus remains negligible compared with the measured ASR. Consequently, the thickness of graphene flakes consisting of up to tens of layers does not introduce a measurable influence on the extracted ASR under conventional visible excitation conditions. This is also true for other 2DM flakes.

5. Conclusion

In summary, we have developed a comprehensive methodology for assessing both LSR and ASR in confocal Raman microscopy by integrating Gaussian beam modeling with systematic cross-edge and z-axial Raman scan measurements on atomically thin 2DMs (graphene and MoS_2) and their underlying Si substrate. Through quantitative analysis of Raman intensity profiles, we elucidated the distinct roles of the 2DM flakes and the Si substrate as reference samples for spatial resolution determination. Our results demonstrate that mono- and multi-layer graphene flakes are universally suitable for LSR calibration, while only monolayer and bilayer MoS_2 are appropriate due to the edge-induced Raman enhancement present in thicker flakes, which distorts the intensity profile. The LSR values extracted from Si substrate were consistently larger than those obtained from 2DM flakes, attributable to the combined effects of the SiO_2 spacer layer and the finite optical penetration depth in Si, which introduce out-of-focus signal contributions. In contrast, the ASR_{exp} values derived from Si substrate showed good agreement with those from 2DM flakes for pinhole sizes larger than 80 μm, despite slight discrepancies under true confocal conditions with small pinholes. By systematically varying the pinhole size from 10 μm to 250 μm, we quantitatively established its influence on both LSR and ASR, confirming that a pinhole size of 20 μm provides optimal confocal conditions for achieving diffraction-limited resolution. The experimental results agree well with theoretical predictions based on the Gaussian beam model, although minor deviations were observed and attributed to the inherent complexity of real optical systems compared to idealized double-lens models. This work not only establishes a robust framework for spatial resolution assessment using 2DMs as ideal reference standards but also provides critical insights into the underlying physical mechanisms governing resolution in confocal Raman microscopy, thereby offering valuable guidance for system optimization and performance evaluation in diverse applications.

Acknowledgements

This work was supported by the National Key Research and Development Program of China (Grant No. 2023YFA1407000), the Strategic Priority Research Program of Chinese Academy of Sciences (Grant No. XDB0460000), the National Natural Science Foundation of China (Grant Nos. 12322401, 12127807, and 12393832), Youth Innovation Promotion Association, Chinese Academy of Sciences (Grant No. 2023125).

References

[1] Jorio A, Dresselhaus M S, Saito R and Dresselhaus G 2011 *Raman Spectroscopy in Graphene Related Systems* (Chichester: John Wiley & Sons)
[2] Tan P H 2019 *Raman Spectroscopy of Two-Dimensional Materials* (Nature Singapore Pte Ltd)
[3] Wu J B, Lin M L, Cong X, Liu H N and Tan P H 2018 *Chem. Soc. Rev.* **47** 1822
[4] Smith E and Dent G 2019 *Modern Raman Spectroscopy: A Practical Approach*, 2nd edn. (Chichester: John Wiley & Sons)
[5] Minsky M (U.S. Patent) 3 013 467 [1961-12-19]
[6] Itoh N 2025 *J. Raman Spectrosc.* **56** 389
[7] Deckert V, Deckert-Gaudig T, Diegel M, Götz I, Langelüddecke L, Schneidewind H, Sharma G, Singh P, Singh P, Trautmann S, Zeisberger M and Zhang Z 2015 *Faraday Discuss.* **177** 9
[8] Richard-Lacroix M, Zhang Y, Dong Z and Deckert V 2017 *Chem. Soc. Rev.* **46** 3922
[9] Glass M and Dabbs T 1991 *J. Microsc.* **164** 153
[10] Pudney P D, Hancewicz T M and Cunningham D G 2002 *J. Spectrosc.* **16** 217
[11] Wermelinger T, Scott S A, Lagally M G, Hinderling C and Spoleank R 2010 *AIP Conf. Proc.* **1267** 776
[12] Lucchese M M, Stavale F, Ferreira E M, Vilani C, Moutinho M O, Capaz R B, Achete C A and Jorio A 2010 *Carbon* **48** 1592
[13] Atkin J M, Berweger S, Jones A C and Raschke M B 2012 *Adv. Phys.* **61** 745
[14] Kolhatkar G, Plathier J and Ruediger A 2018 *J. Mater. Chem. C* **6** 1307
[15] Nehrke G and Nouet J 2011 *Biogeosciences* **8** 3761
[16] Leimhofer C, Hammer A, Roland W and Hild S 2023 *AIP Conf. Proc.* **2607** 020011
[17] Kuball M and Pomeroy J W 2016 *IEEE Trans. Device Mater. Reliab.* **16** 667
[18] Sammon C, Mura C, Eaton P and Yarwood J 2000 *Analusis* **28** 30
[19] De Wolf I, Maes H and Jones S K 1996 *J. Appl. Phys.* **79** 7148
[20] Muller M 2006 *Introduction to Confocal Fluorescence Microscopy* (Bellingham: SPIE Press)
[21] Kim Y, Lee E J, Roy S, Sharbirin A S, Ranz L G, Dieing T and Kim J 2020 *Curr. Appl. Phys.* **20** 71
[22] Bereczki A, Dipold J, Freitas A Z and Wetter N U 2023 *Polymers* **15** 4644
[23] Park J, Kim J and Kwon H 2020 *Bull. Korean Chem. Soc.* **41** 34
[24] Suzaki Y and Tachibana A 1975 *Appl. Opt.* **14** 2809

[25] Hauer P, Grand J, Djorovic A, Willmott G and Le Ru E 2016 *J. Phys. Chem. C* **120** 21104

[26] Fu Y Z, Ding X, Li J C and Zhang J Y 2019, *AOPC 2019: Optical Spectroscopy and Imaging* 7–9 July 2019, Beijing, China. SPIE 11337 11337B

[27] Liu T, Lin M L, Meng D, Cong X, Kan Q, Wu J B and Tan P H 2025 *Chin. Phys. B* **34** 017801

[28] Khorasaninejad M, Walia J and Saini S S 2013 *Appl. Phys. Lett.* **103** 163110

[29] Poborchii V, Tada T and Kanayama T 2009 *Appl. Phys. Lett.* **94** 131907

[30] Sacco A, Portesi C, Giovannozzi A M and Rossi A M 2021 *J. Raman Spectrosc.* **52** 1671

[31] Wang Z J, Liu T, Liu X L, Lin M L and Tan P H 2026 *Rev. Sci. Instrum.* **97** 023702

[32] Brakenhoff G J, van der Voort H T M, van Spronsen E A and Nanninga N 1986 *Ann. N. Y. Acad. Sci.* **483** 405

[33] Puppels G J, Colier W, Olminkhof J H E, Otto C, De Mul F F M and Greve J 1991 *J. Raman Spectrosc.* **22** 217

[34] de Grauw C J, Sijtsema N M, Otto C and Greve J 1997 *J. Microsc.* **188** 273

[35] Korzeniewski C, Kitt J P, Bukola S, Creager S E, Minteer S D and Harris J M 2019 *Anal. Chem.* **91** 1049

[36] [36] Castellanos-Gomez A, Buscema M, Molenaar R, Singh V, Janssen L, van der Zant H S J and Steele G A 2014 *2D Mater.* **1** 011002

[37] Li X L, Qiao X F, Han W P, Lu Y, Tan Q H, Liu X L and Tan P H 2015 *Nanoscale* **7** 8135

[38] Li X L, Qiao X F, Han W P, Zhang X, Tan Q H, Chen T and Tan P H 2016 *Nanotechnology* **27** 145704

[39] Chen X, Lin M L, Cong X, Leng Y C, Zhang X and Tan P H 2021 *Carbon* **185** 282

[40] Zhang X, Han W, Wu J, Milana S, Lu Y, Li Q, Ferrari A and Tan P 2013 *Phys. Rev. B* **87** 115413

[41] Lenferink A and Otto C 2025 *J. Microsc.* **300** 124

[42] Quimby R S 2006 *Photonics and Lasers: An Introduction* (Hoboken: John Wiley & Sons) Chapter 17 pp. 307–325

[43] International Organization for Standardization 2019 *Surface Chemical Analysis—Determination of Lateral Resolution and Sharpness in Beam Based Methods with a Range from Nanometres to Micrometres* (Geneva: International Organization for Standardization) ISO 18516:2019

[44] Wilson T 2011 *J. Microsc.* **244** 113

[45] Wilson T 1989 *J. Microsc.* **154** 143

[46] Everall N J 2000 *Appl. Spectrosc.* **54** 773